

Transition from fishbone mode to β -induced Alfvén eigenmode on HL-2A tokamak

Zhihui Zou¹, Ping Zhu^{2,3*}, Charlson C. Kim⁴, Xianqu Wang⁵, Yawei Hou^{1**}

¹ CAS Key Laboratory of Geospace Environment and Department of Plasma Physics and Fusion Engineering, University of Science and Technology of China, Hefei, Anhui 230026, China

² International Joint Research Laboratory of Magnetic Confinement Fusion and Plasma Physics, State Key Laboratory of Advanced Electromagnetic Engineering and Technology, School of Electrical and Electronic Engineering, Huazhong University of Science and Technology, Wuhan, Hubei 430074, China

³ Department of Engineering Physics, University of Wisconsin-Madison, Madison, Wisconsin 53706, USA

⁴ SLS2 Consulting, San Diego, California 92107, USA

⁵ Institute of Fusion Science, School of Physical Science and Technology, Southwest Jiaotong University, Chengdu, Sichuan 610031, China

* Corresponding author 1 Ping Zhu: zhup@hust.edu.cn

** Corresponding author 2 Yawei Hou: arvayhou@ustc.edu.cn

Abstract

In the presence of energetic particles (EPs) from auxiliary heating and burning plasmas, fishbone instability and Alfvén modes can be excited and their transition can take place in certain overlapping regimes. Using the hybrid kinetic-magnetohydrodynamic model in the NIMROD code, we have identified such a transition between the fishbone instability and the β -induced Alfvén Eigenmode (BAE) for the NBI heated plasmas on HL-2A. When the safety factor at magnetic axis is well below one, typical kink-fishbone transition occurs as the EP fraction increases. When q_0 is raised to approaching one, the fishbone mode is replaced with BAE for sufficient amount of EPs. When q_0 is slightly above one, the toroidicity-induced Alfvén eigenmode (TAE) dominates at lower EP pressure, whereas BAE

dominates at higher EP pressure.

Keywords: internal kink mode, fishbone mode, β -induced Alfvén eigenmode(BAE), energetic particles(EPs), HL-2A, NIMROD

1 Introduction

Energetic particles (EPs) produced from auxiliary heating and burning plasmas are known to have strong influence on the internal 1/1 kink [1–3] and Alfvén eigenmodes [4] in tokamaks. In particular, the fishbone modes have been observed widely on tokamaks, such as PDX [10], DIII-D [5], JET [6], HL-2A [7], and EAST [8], in the presence of Neutral Beam Injection (NBI), Electron Cyclotron Resonant Heating (ECRH), or Ion Cyclotron Resonant Heating (ICRH), which are believed to be driven by the resonance between the trapped EPs and the internal kink modes, along with the diamagnetic dissipations from the EPs [11, 12]. On the other hand, various Alfvén eigenmodes (AEs), either in the spectral gap or on the continuum, can be excited by the EPs. Whereas the EP driven mechanisms for each of the individual MHD and AE instabilities have been intensively studied [13–17], their overlapping regimes or transition conditions have been less clear.

HL-2A is a medium-sized tokamak where, with ECRH and NBI heatings, a number of EP driven instabilities, such as ion-fishbone [22], e-fishbone [23], TAE [24], and BAE [25], have been observed. Based on the HL-2A configuration, we have recently found an overlapping regime and condition for the transition from fishbone to BAE instabilities in the presence of EPs, using the hybrid kinetic-MHD (HK-MHD) model implemented in the NIMROD code [27, 28]. With continuous variation of the safety factor profile and the EP β fraction, the dispersion relation and mode structure of the dominant EP-driven instability alternate between the characteristics of the fishbone and the Alfvén modes. The overlapping or adjacency for the regimes of these two distinctively different EP modes

may not be always guaranteed, and our findings may help their identification and interpretation in experiments.

The rest of paper is organized as follows. The simulation model is reviewed briefly in section 2. The simulation set-up is described in section 3, which is followed by the report on the main results in section 4. Finally, we conclude with a summary and discussion in section 5.

2 Simulation model

The HK-MHD equations implemented in the NIMROD code including EP effects are as follows [28]

$$\frac{\partial \rho}{\partial t} + \nabla \cdot (\rho \mathbf{V}) = 0 \quad (1)$$

$$\rho \left(\frac{\partial \mathbf{V}}{\partial t} + \mathbf{V} \cdot \nabla \mathbf{V} \right) = \mathbf{J} \times \mathbf{B} - \nabla p_b - \nabla \cdot \mathbf{P}_h \quad (2)$$

$$\frac{n}{\gamma - 1} \left(\frac{\partial T}{\partial t} + \mathbf{V} \cdot \nabla T \right) = 0 \quad (3)$$

$$\frac{\partial \mathbf{B}}{\partial t} = -\nabla \times \mathbf{E} \quad (4)$$

$$\mu_0 \mathbf{J} = \nabla \times \mathbf{B} \quad (5)$$

$$\mathbf{E} = -\mathbf{V} \times \mathbf{B} \quad (6)$$

where ρ , \mathbf{V} , \mathbf{J} , \mathbf{B} , p_b , and \mathbf{E} are the mass density, center of mass velocity, current density, magnetic field, background pressure, and electric field respectively. In the limits of $n_h \ll n_b$, $\beta_h \sim \beta_b$, where n_b (n_h) is the background plasma (energetic particle) number density, β_b (β_h) is the ratio of background plasma (energetic particle) pressure to magnetic pressure, and the kinetic effect of EP is coupled into MHD equations by adding EP pressure tensor \mathbf{P}_h to the momentum equation. The drift-kinetic equation is solved to determine the EP distribution and the pressure tensor \mathbf{P}_h [28].

3 Simulation setup

The equilibrium is constructed from HL-2A discharge #16074 using EFIT [31]. The equilibrium flux surfaces and the mesh grid in magnetic flux coordinates are shown in FIG 1, where the last closed flux surface (LCFS) is up-down asymmetric, and the flux surfaces are close to circles in the core region. As can be seen in FIG 2(a), the q profile is rather flat about one in the core region $0 < \sqrt{\psi/\psi_0} < 0.2$,

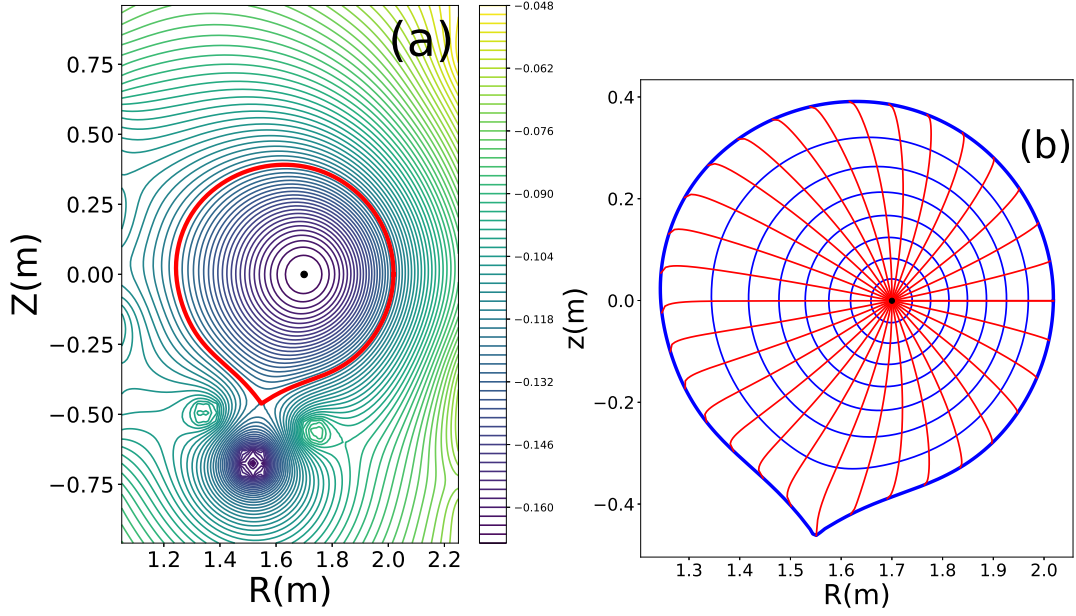


Figure 1: (a) Contour plot of equilibrium poloidal flux in (R, Z) coordinate. The red curve represents the last closed flux surface (LCFS). (b) The mesh grid of flux coordinates used in the Alfvén continuum calculation. Uniform poloidal flux and equal poloidal arc length are used in this flux coordinate system. The black point locates at the magnetic axis. The blue lines represent the constant poloidal fluxes, and the red lines the constant poloidal angles. The mesh grids used in the actual calculation are much finer than the above diagram.

where ψ is the poloidal magnetic flux, and ψ_0 is the total poloidal magnetic flux within the LCFS. The slowing-down distribution function is used for the EPs,

$$f_0 = \frac{P_0 \exp\left(\frac{P_\zeta}{\psi_n}\right)}{\epsilon^{3/2} + \epsilon_c^{3/2}} \quad (7)$$

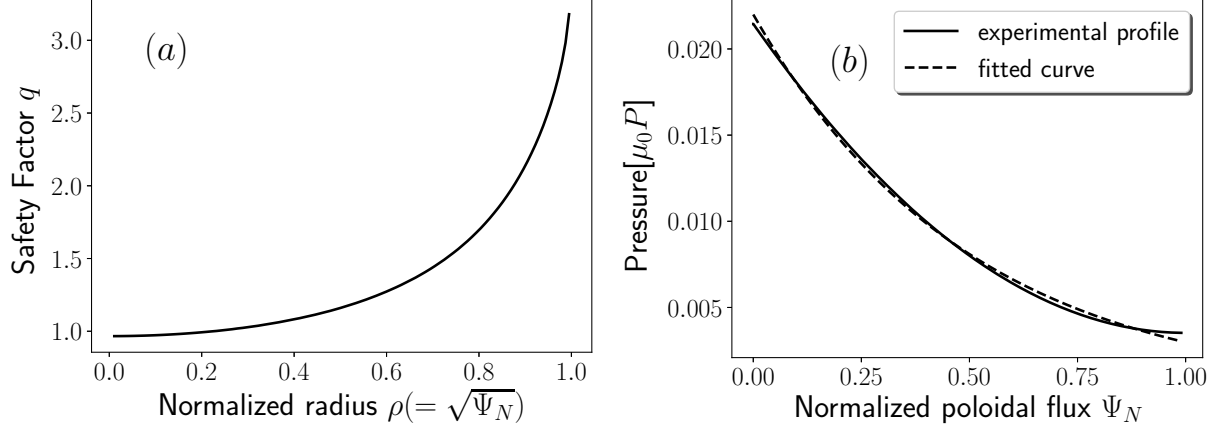


Figure 2: (a) q -profile and (b) pressure profiles in HL-2A discharge #16074.

where P_0 is the normalization constant, $P_\zeta = g\rho_{\parallel} - \psi_p$ is the canonical toroidal momentum, $g = RB_\phi$, $\rho_{\parallel} = mv_{\parallel}/qB$, ψ_p is the poloidal flux, $\psi_n = c\psi_0$, ψ_0 is the total flux and the parameter c is used to match the spatial profile of the equilibrium, ε is the particle energy, and ε_c is the critical slowing down energy [30]

$$\varepsilon_c = \left(\frac{3}{4}\right)^{2/3} \left(\frac{\pi m_i}{m_e}\right)^{1/3} T_e \quad (8)$$

with m_i being the ion mass, m_e the electron mass, and T_e the electron temperature. When $\varepsilon > \varepsilon_c$, the slowing down of beam ions is mainly due to the collisions with background electrons, and the collisions with background ions is dominant when $\varepsilon < \varepsilon_c$. As the beam ions slow down, they give up their energy increasingly to the background ions, rather than to the background electrons. The slowing down distribution models the process which is dominated by the collisions between beam ions and background ions.

As shown in FIG 2(b), the energetic particles are loaded into the physical space following the profile $p = p_0 \exp(-c\psi/\psi_0)$, where p_0 is pressure at magnetic axis, $c = 0.5$. Parameters p_0 and c are generated from the fitting to the original pressure profile from experiment. Other main parameters are set up as follows [32]. The major radius $R = 1.65\text{m}$, and the minor radius $a = 0.40\text{m}$ for the LCFS, the toroidal magnetic field $B_0 = 1.37\text{T}$, the number density $n = 2.44 \times 10^{19}\text{m}^{-3}$, the initial energy of

beam ions is $\varepsilon_m = 40\text{keV}$, the background electron temperature $T_e = 1\text{keV}$, and according to equation (8), the critical energy is $\varepsilon_c = 14.8\text{keV}$.

4 Simulation results

4.1 Effects of q_0 in absence of energetic particles

In absence of energetic particles, we find in NIMROD calculations that the $(m, n) = (1, 1)$ mode is the most unstable, where n and m are the toroidal and the poloidal mode numbers respectively. Only

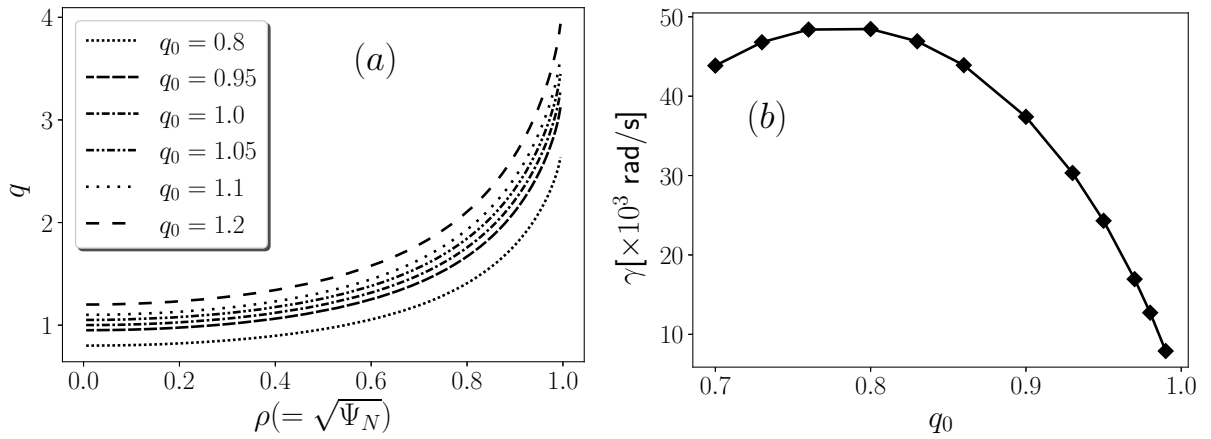


Figure 3: (a) q -profiles with different q_0 and (b) the growth rates dependence on q_0 for $(m, n) = (1, 1)$ modes.

the safety factor q_0 at magnetic axis is varied, so that the q -profile shifts up or down entirely without changing its shape (FIG. 3a). The linear growth rate of the $(1, 1)$ mode from NIMROD calculations increases first before decreases, and approaches 0 as q_0 approaches to unity. The growth rate of $(1, 1)$ modes reaches its maximum at $q_0 = 0.77$.

Such a dependence of growth rate on q_0 may be understood from previous theory [3]. For a monotonic parabolic q -profile with q_0 below 1, the distance $|1 - q_0|$ can be seen as a measure of free

energy within the $q = 1$ surface from equation

$$\gamma = -\frac{r_0 V_A \pi \delta W_T}{\sqrt{3} R_0 R_0 q'} \quad (9)$$

$$\delta W_T \sim 3\nu \Delta q \left[\frac{13}{48(\nu + 4)} - \beta_p^2 \int_{r_0}^{r^2} \frac{dr}{r_0} \left(\frac{r}{r_0} \right)^{\nu-5} \right] \quad (10)$$

where $\Delta q = 1 - q_0$, $1 - q(r) \sim \Delta q [1 - (r/r_0)^\nu]$, $q(r_0) = 1$, V_A is Alfvén velocity, R_0 is the major radius at magnetic axis, and $\beta_p = [2\mu_0/B_p^2(r_0)] \int_0^{r_0} (r/r_0)^2 (-dp/dr)$ is poloidal beta. It follows that the free energy decreases with q_0 ($q_0 < 1$). The magnetic shear $q' = dq/dr$ and the toroidal potential energy δW_T (free energy) can stabilize and destabilize the mode respectively. As q_0 increases, both the magnetic shear q' and the toroidal potential energy δW_T decrease. At first, the decreasing of stabilizing effect from the magnetic shear q' is dominant, so the growth rate increases; as q_0 increases further, the reduction of toroidal potential energy δW_T becomes dominant, so the growth rate starts to decrease.

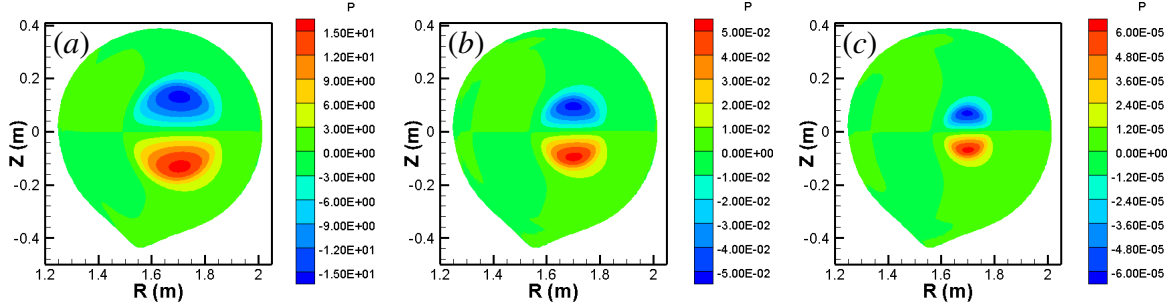


Figure 4: Contour plots of pressure perturbation for different q_0 : (a) $q_0 = 0.80$, (b) $q_0 = 0.90$, and (c) $q_0 = 0.95$.

The contour plots of the plasma pressure perturbation show that the $(1, 1)$ mode structure shrinks in size and becomes more localized in the core region as q_0 approaches to 1, which further confirms the theory prediction in Equations (9) and (10).

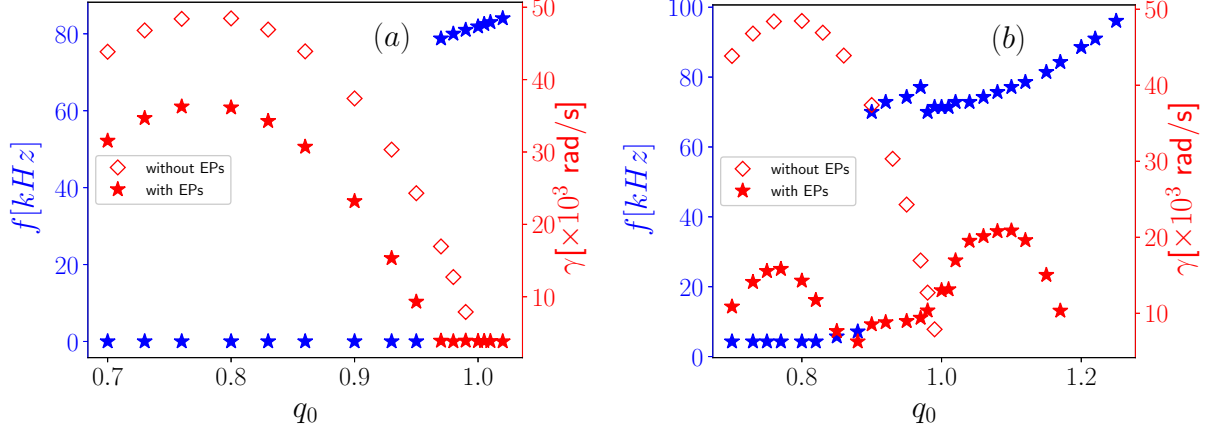


Figure 5: The frequency and growth rate dependence on q_0 for (1, 1) modes. (a) $\beta_h/\beta_0 = 0.25$ and (b) $\beta_h/\beta_0 = 0.5$.

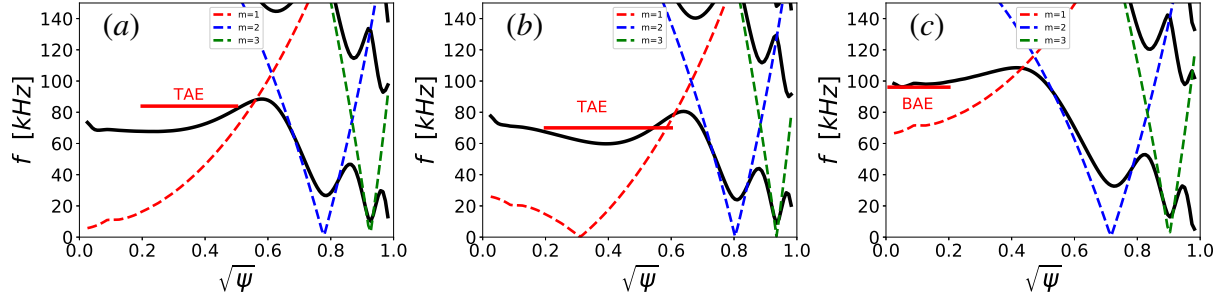


Figure 6: Alfvén continua with toroidal mode number $n = 1$ calculated based on the slow-sound approximation from AWEAC. Alfvén continua from the cylindrical geometry limit (dotted line) are also given. (a) $\beta_h/\beta_0 = 0.25$, $q_0 = 1.02$; (b) $\beta_h/\beta_0 = 0.5$, $q_0 = 0.90$; and (c) $\beta_h/\beta_0 = 0.5$, $q_0 = 1.25$.

4.2 Effects of q_0 in the presence of energetic particles

In the presence of EPs with $\beta_h/\beta_0 = 25\%$, the growth rate of (1, 1) mode increases first and then decreases as q_0 increases (FIG. 5a). Comparison with the cases without EPs indicates that the dependence of growth rate on q_0 is similar whereas the EPs have an overall stabilizing effect. The frequency is almost constant (3kHz) when $q_0 < 0.95$, which can be identified as that of the fishbone mode. For $q_0 > 0.95$, the mode frequency jumps to another branch around 80kHz and increases with q_0 , which is considered as a TAE from the Alfvénic continua in FIG. 6(a). For higher EP fraction

with $\beta_h/\beta_0 = 50\%$, the transition from the fishbone branch to the TAE branch takes place at a lower $q_0 \simeq 0.88$, and the transition from the TAE branch to the BAE branch happens at $q_0 \simeq 0.97$, and the significantly enhanced BAE growth rate reaches its maximum around $q_0 = 1.1$ (FIG. 5b).

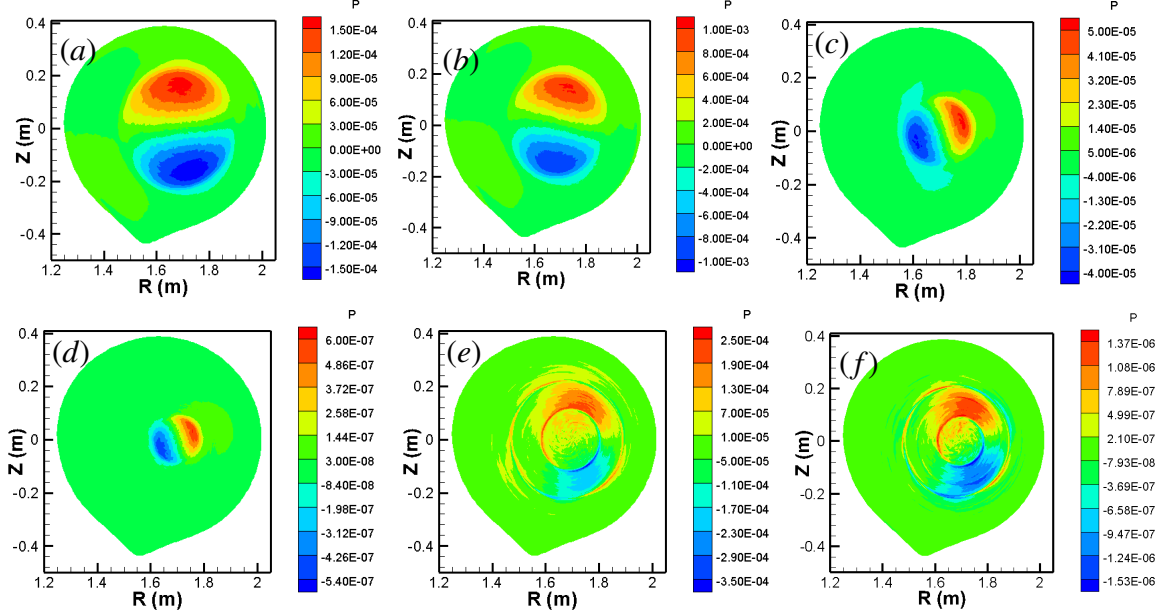


Figure 7: Contour plots of pressure perturbation of $n = 1$ mode in poloidal plane with $\beta_h/\beta_0 = 25\%$ and (a) $q_0 = 0.70$, (b) $q_0 = 0.77$, (c) $q_0 = 0.90$, (d) $q_0 = 0.95$, (e) $q_0 = 1.02$, and (f) $q_0 = 1.05$.

The dominant modes transition is also evident from the variation of mode structure with q_0 . For example, in the case with $\beta_h/\beta_0 = 0.25$, the perturbed pressure contour for the $n = 1$ mode in the poloidal plane shows clear $(1, 1)$ kink mode structure inside the $q = 1$ surface when $q_0 < 0.95$, which shrinks in size as q_0 increases (FIG. 7a~d). When $q_0 > 0.95$, the mode structure becomes qualitatively different, which now involves the coupling between two rational surfaces, which is characteristic of the TAE mode (FIG. 7e~f).

4.3 Effects of energetic particles for different q_0

For cases with $q_0 = 0.77$, as the EP fraction $\beta_f = \beta_h/\beta_0$ increases, the growth rate decreases first before rising again, whereas the real frequency grows about linearly in both regimes. The transition

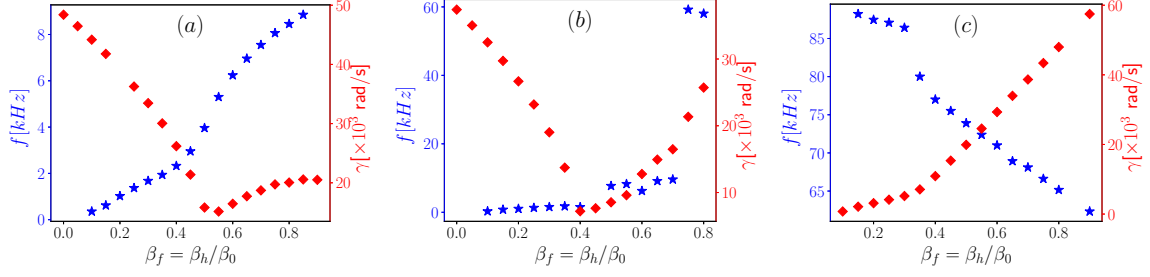


Figure 8: The frequency and growth rate dependence on $\beta_f = \beta_h/\beta_0$ with (a) $q_0 = 0.77$, (b) $q_0 = 0.9$, and (c) $q_0 = 1.05$.

between the two regimes occurs at $\beta_f = 0.57$. When the EP pressure is in the relatively low regime, the stabilizing effect of EP on the kink mode is dominant; in the relatively high EP pressure regime, fishbone mode can be excited. These results are consistent with previous theories [18, 33] and simulations [28, 34]. When $q_0 = 0.90$, the growth rate has the similar dependence on β_h/β_0 , with a lower transitional threshold $\beta_h/\beta_0 = 0.4$. However, in higher β_f regime, a new mode branch appears where the real frequency is distinctively higher and decreases with β_f . For $q_0 = 1.05$, only the new mode branch persists, where the growth rate increases and the real frequency decreases with β_f .

In order to identify the nature of the higher frequency mode, we vary the specific heat coefficient Γ of the bulk plasma, and calculate the growth rate. From FIG. 9 (b), we can see that, when $q_0 = 0.9$ and $\beta_h/\beta_0 = 0.8$, the square of mode frequency increases linearly with Γ , which is consistent with the property of BAE [21]. Similarly, the BAE nature of the is also verified for $q_0 = 1.05$ and $\beta_h/\beta_0 = 0.8$ (FIG. 9c). In contrast, for $q_0 = 0.77$ and $\beta_h/\beta_0 = 0.8$, no apparent relation between the mode frequency and Γ can be found, where the fishbone mode dominates (FIG. 9a). Based on the Alfvén continua for toroidal mode number $n = 1$ calculated using the AWEAC code, the radial locations and frequencies of the modes with $q_0 = 0.9$ and $q_0 = 1.05$ are well within the BAE gap (FIG. 10).

As both q_0 and β_f increase from the kink dominant regime, the transition to BAE dominant regime is also apparent in the variation of mode structure (FIG. 11). In the lower q_0 and β_f regime, the well-defined (1, 1) kink mode structure is localized inside the $q = 1$ surface (FIG. 11a). This contrasts

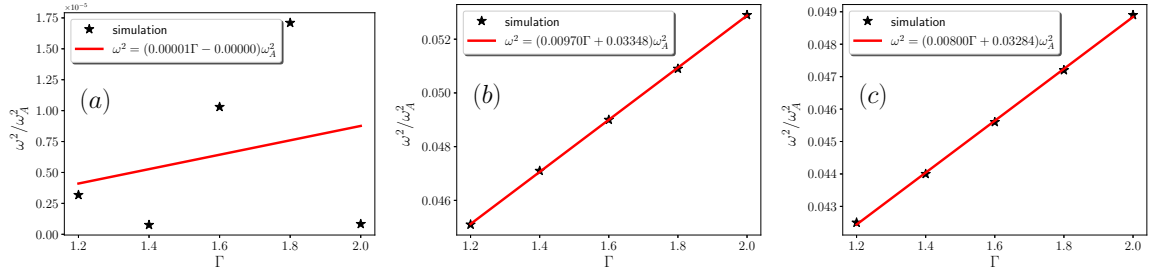


Figure 9: The square of normalized mode frequency as a function of the specific heat coefficient Γ for (a) $q_0 = 0.77$; (b) $q_0 = 0.9$; and (c) $q_0 = 1.05$.

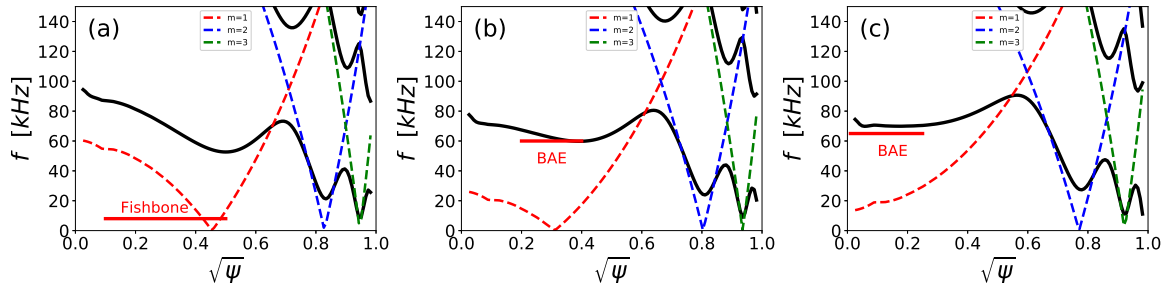


Figure 10: Alfvén continua with toroidal mode number $n = 1$ calculated based on the slow-sound approximation from AWEAC. Alfvén continua from the cylindrical geometry limit (dotted line) are also given. (a) $q_0 = 0.77$; (b) $q_0 = 0.9$; and (c) $q_0 = 1.05$.

with the multiple-surface coupled mode structure for BAE in the higher q_0 and β_f regime (FIG. 11i). In between, the transition manifests in the mixture of the characteristics of both kink and AE modes (e.g. FIG. 11f).

5 Conclusions

In summary, the transition of the dominant $n = 1$ mode from fishbone to BAE instability in the HL-2A tokamak configuration has been observed to take place when both the safety factor q_0 at magnetic axis and the energetic particle fraction are above certain threshold in hybrid-kinetic MHD simulations using the NIMROD code. When q_0 is well below unity, the dominant EP-driven instability is the

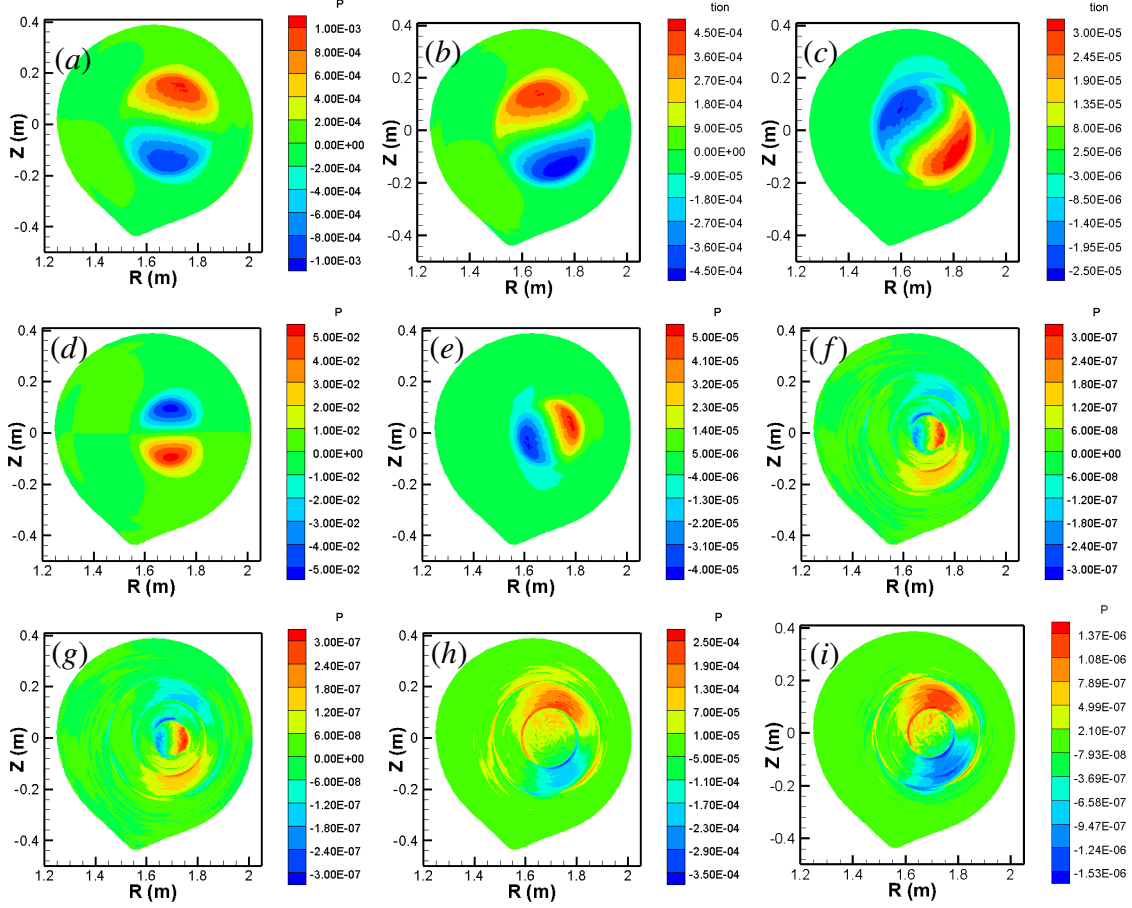


Figure 11: Contour plot of plasma pressure with (a) $q_0 = 0.77, \beta_h/\beta_0 = 0.25$, (b) $q_0 = 0.77, \beta_h/\beta_0 = 0.5$, (c) $q_0 = 0.77, \beta_h/\beta_0 = 0.75$, (d) $q_0 = 0.9, \beta_h/\beta_0 = 0.25$, (e) $q_0 = 0.9, \beta_h/\beta_0 = 0.50$, (f) $q_0 = 0.9, \beta_h/\beta_0 = 0.75$, (g) $q_0 = 1.05, \beta_h/\beta_0 = 0.25$, (h) $q_0 = 1.05, \beta_h/\beta_0 = 0.5$, and (i) $q_0 = 1.05, \beta_h/\beta_0 = 0.75$.

fishbone mode; when q_0 is slightly above unity, the dominant EP-driven instability becomes TAE and BAE as the EP fraction increases. The transition occurs in between these two regimes, where the mode frequency experiences abrupt jump even though the mode growth rate varies continuously, and the mode structure shows a mixture of signatures from both kink-fishbone and TAE/BAE. These findings may help the identification and control of the dominant EP-driven modes in experiments.

For the HL-2A experimental equilibrium we study in this work, the q profile is rather flat in the core region. The effects of the weak magnetic shear on the EP-driven modes remain to be better understood. In addition, as the EP fraction of plasma β increases, the finite orbit size of EP may no

longer be ignored. We plan on further addressing these issues in future work.

Acknowledgments

This work was supported by the National Magnetic Confinement Fusion Program of China Grant No. 2019YFE03050004, the National Natural Science Foundation of China Grant Nos. 11875253, 11775221, 51821005, the Fundamental Research Funds for the Central Universities Grant Nos. WK3420000004 and 2019kfyXJJS193, the Collaborative Innovation Program of Hefei Science Center, CAS Grant No. 2019HSC-CIP015, the U.S. Department of Energy Grant Nos. DE-FG02-86ER53218 and DE-SC0018001. This research used the computing resources from the Supercomputing Center of University of Science and Technology of China.

References

- [1] Shafranov V D 1970 *Soviet Physics Technical Physics* **15** 175
- [2] Rosenbluth M N *et al* 1973 *Physics of Fluids* **16** 1894
- [3] Bussac M N *et al* 1975 *Physical Review Letters* **35** 1638
- [4] Fasoli A *et al* 2007 *Nuclear Fusion* **47** S264
- [5] Heidbrink W W and Sager G 1990 *Nuclear Fusion* **30** 1015
- [6] Nave M *et al* 1991 *Nuclear Fusion* **31** 697
- [7] Chen W *et al* 2010 *Nuclear Fusion* **50** 084008
- [8] Xu L Q *et al* 2015 *Physics of Plasmas* **22** 122510
- [9] Von Goeler S *et al* 1974 *Physical Review Letters* **33** 1201

- [10] McGuire K *et al* 1983 *Physical Review Letters* **50** 891
- [11] Chen L *et al* 1984 *Physical Review Letters* **52** 1122
- [12] Coppi B and Porcelli F 1986 *Physical Review Letters* **57** 2272
- [13] Rosenbluth M N and Rutherford P H 1975 *Physical Review Letters* **34** 1428
- [14] Tsang K T *et al* 1981 *The Physics of Fluids* **24** 1508
- [15] Fu G Y and Van Dam J W 1989 *Physics of Fluids B: Plasma Physics* **1** 1949
- [16] Fu G Y and Van Dam J W 1989 *Physics of Fluids B: Plasma Physics* **1** 2404
- [17] Chen L and Zonca F 2016 *Reviews of Modern Physics* **88** 015008
- [18] White R B *et al* 1989 *Physical Review Letters* **62** 539
- [19] Cheng C Z and Chance M S 1986 *The Physics of Fluids* **29** 3695
- [20] Heidbrink W W *et al* 1993 *Physical Review Letters* **71** 855
- [21] Shen W *et al* 2017 *Nuclear Fusion* **57** 116035
- [22] Chen W *et al* 2018 *Nuclear Fusion* **58** 014001
- [23] Yu L M *et al* 2013 *Nuclear Fusion* **53** 053002
- [24] Yu L M *et al* 2018 *Physics of Plasmas* **25** 012112
- [25] Shi P W *et al* 2019 *Nuclear Fusion* **59** 066015
- [26] Ding X T and Chen W 2018 *Plasma Science and Technology* **20** 094008
- [27] Sovinec C R *et al* 2004 *Journal of Computational Physics* **195** 355
- [28] Kim C C and the NIMROD team 2008 *Physics of Plasmas* **15** 072507

- [29] Hou Y W *et al* 2019 *Physics of Plasmas* **26** 082505
- [30] Goldston R J and Rutherford P H *Introduction to Plasma Physics* 2000 (Institute of Physics, Philadelphia)
- [31] Deng W *et al* 2014 *Nuclear Fusion* **54** 013010
- [32] Zhang R B *et al* 2014 *Plasma Physics & Controlled Fusion* **56** 095007
- [33] Wu Y L *et al* 1994 *Physics of Plasmas* **1** 3369
- [34] Fu G Y *et al* 2006 *Physics of Plasmas* **13** 052517